



Observations of the Disk/Jet Coupling of MAXI J1820+070 during Its Descent to Quiescence

A. W. Shaw¹ , R. M. Plotkin¹ , J. C. A. Miller-Jones² , J. Homan^{3,4} , E. Gallo⁵ , D. M. Russell⁶ , J. A. Tomsick⁷ , P. Kaaret⁸ , S. Corbel^{9,10} , M. Espinasse⁹ , and J. Bright¹¹

¹ Department of Physics, University of Nevada, Reno, NV 89557, USA; aarrans@unr.edu

² International Centre for Radio Astronomy Research, Curtin University, GPO Box U1987, Perth, WA 6845, Australia

³ Eureka Scientific, Inc., 2452 Delmer Street, Oakland, CA 94602, USA

⁴ SRON Netherlands Institute for Space Research, Sorbonnelaan 2, NL-3584 CA Utrecht, The Netherlands

⁵ Department of Astronomy, University of Michigan, 1085 S University, Ann Arbor, MI 48109, USA

⁶ Center for Astro, Particle and Planetary Physics, New York University Abu Dhabi, P.O. Box 129188, Abu Dhabi, UAE

⁷ Space Sciences Laboratory, 7 Gauss Way, University of California, Berkeley, CA 94720-7450, USA

⁸ Department of Physics and Astronomy, University of Iowa, Iowa City, IA 52242, USA

⁹ AIM, CEA, CNRS, Université de Paris, Université Paris-Saclay, F-91191 Gif-sur-Yvette, France

¹⁰ Station de Radioastronomie de Nançay, Observatoire de Paris, PSL Research University, CNRS, Univ. Orléans, F-18330 Nançay, France

¹¹ Astrophysics, Department of Physics, University of Oxford, Keble Road, Oxford, OX1 3RH, UK

Received 2020 September 8; revised 2020 December 4; accepted 2020 December 7; published 2021 January 25

Abstract

Black hole X-ray binaries in the quiescent state (Eddington ratios typically $\lesssim 10^{-5}$) display softer X-ray spectra (photon indices $\Gamma \sim 2$) compared to higher-luminosity black hole X-ray binaries in the hard state ($\Gamma \sim 1.7$). However, the cause of this softening and its implications for the underlying accretion flow are still uncertain. Here, we present quasi-simultaneous X-ray and radio spectral monitoring of the black hole X-ray binary MAXI J1820 +070 during the decay of its 2018 outburst and of a subsequent reflare in 2019, providing an opportunity to monitor a black hole X-ray binary as it actively transitions into quiescence. We probe 1–10 keV X-ray luminosities as low as $L_X \sim 4 \times 10^{32}$ erg s⁻¹, equivalent to Eddington fractions of $\sim 4 \times 10^{-7}$. During its decay toward quiescence, the X-ray spectrum of MAXI J1820+070 softens from $\Gamma \sim 1.7$ to $\Gamma \sim 2$, with the softening taking ~ 30 days and completing at $L_X \approx 10^{34}$ erg s⁻¹ ($\approx 10^{-5} L_{\text{Edd}}$). While the X-ray spectrum softens, the radio spectrum generally remains flat or inverted throughout the decay. We also find that MAXI J1820+070 follows a radio (L_R)–X-ray luminosity correlation of the form $L_R \propto L_X^{0.52 \pm 0.07}$, making it the fourth black hole system to follow the so-called “standard track” unbroken over several (in this case, four) decades in L_X . Comparing the radio/X-ray spectral evolution(s) with the L_R – L_X plane, we find that the X-ray softening is consistent with X-rays produced by Comptonization processes in a radiatively inefficient accretion flow. We generally disfavor X-ray emission originating solely from within the jet, with the possible exception of X-rays produced via synchrotron self-Compton processes.

Unified Astronomy Thesaurus concepts: Black holes (162); Accretion (14); Low-mass x-ray binary stars (939); X-ray transient sources (1852)

1. Introduction

Black hole low-mass X-ray binaries (BH-LMXBs) are binary systems containing a black hole (BH) accreting matter from a low-mass ($\lesssim 1\text{--}2M_\odot$) stellar companion. Most BH-LMXBs are transients, spending long periods of time in a quiescent state, exhibiting very low accretion rates, followed by bright outbursts during which the source luminosity increases by several orders of magnitude (see, e.g., Remillard & McClintock 2006; Tetarenko et al. 2016) across the majority of the electromagnetic spectrum. During these outbursts, BH-LMXBs typically transition through a series of “accretion states,” often spending several months in a soft X-ray spectral state characterized by disk-dominated soft X-ray spectra and little to no detectable radio emission. A transition to a hard X-ray state is marked with the emergence of persistent compact radio emission with a flat or inverted spectrum often extending to the infrared regime (e.g., Fender 2001; Corbel & Fender 2002; Russell et al. 2013), interpreted as emission from a partially self-absorbed synchrotron jet. The compact jet may become increasingly important as BH-LMXBs fade to lower luminosities, where the jet’s mechanical power might account for a substantial fraction of the total accretion power (Fender et al. 2001, 2003). BH-LMXBs in the hard state exhibit X-ray spectra

consistent with inverse-Compton scattering of photons off hot electrons, manifesting as a hard power law with a high-energy cutoff (see, e.g., Remillard & McClintock 2006; Done et al. 2007; Belloni 2010, for reviews of accretion states).

In the quiescent state, BH-LMXBs are observed to have softer X-ray spectra compared to the hard state (e.g., Tomsick et al. 2001; Kong et al. 2002; Tomsick et al. 2004; Corbel et al. 2006; Reynolds et al. 2014), with the spectral softening probably occurring at X-ray luminosity $L_X \lesssim 10^{-4} L_{\text{Edd}}$ and typically completing by $L_X \sim 10^{-5} L_{\text{Edd}}$, where L_{Edd} is the Eddington luminosity, at which point the spectral shape remains constant as the luminosity continues to decrease (Sobolewska et al. 2011; Plotkin et al. 2013, 2017b). However, the cause of the softening remains unknown, as observations with the sensitivities required to accurately measure the spectrum of BH-LMXBs as they approach quiescent luminosities are rare.

At the lowest luminosities, it is generally accepted that most (but not necessarily all) of the X-ray emission is produced by a radiatively inefficient mechanism, for both accretion flow and jet-related origins (e.g., Blandford & Begelman 1999; Markoff et al. 2003, 2005; Narayan & McClintock 2008; Yuan & Narayan 2014). There are a number of varieties of radiatively inefficient accretion

flow (RIAF) models, which generally predict that, as luminosity decreases, there will be a gradual increase of the X-ray power-law photon index (Γ). The softening is generally due either to a lower optical depth to inverse-Compton scattering or to a lower average energy change per inverse-Compton scatter (Esin et al. 1997).

Thus, in the context of an RIAF, as a BH-LMXB fades from the hard state into quiescence, there should be fewer hard X-rays emitted (see also Veledina et al. 2011).¹²

On the other hand, it is also possible for synchrotron or synchrotron self-Compton (SSC) emission from a jet to contribute to the X-ray emission (e.g., Markoff et al. 2005; Yuan & Cui 2005; Corbel et al. 2008; Plotkin et al. 2012), and there are several scenarios where jetted X-ray emission could explain the X-ray softening between the hard state and quiescence. If X-rays are produced by optically thin synchrotron radiation from nonthermal particles, then from most diffusive shock acceleration scenarios (e.g., Jones & Ellison 1991) one would expect X-ray photon indices of $\Gamma \approx 1.5\text{--}1.7$ in the hard state. Then, the X-ray softening in quiescence could be explained by increased radiative losses, since a synchrotron-cooled jet would produce a steeper X-ray spectrum (Heinz 2004). Alternatively, if radiative losses are never significant, then less efficient particle acceleration could be invoked (i.e., the synchrotron-emitting particle distribution steepens with decreasing luminosity) or SSC processes from particles accelerated along the jet or thermal particles in the base of the jet. In the SSC case, a spectral softening could occur if a softer spectrum of seed photons is upscattered into the X-ray wave band (see, e.g., Corbel et al. 2008; Plotkin et al. 2015, 2017b; Connors et al. 2017, for discussions on particle acceleration and SSC).

Although models that suggest jet emission may contribute some level of X-ray emission have shown promise (e.g., Markoff et al. 2001, 2003; Plotkin et al. 2015; Connors et al. 2017), this is still a matter of debate (e.g., Zdziarski et al. 2003; Maccarone 2005; Malzac et al. 2009). Progress in clarifying the dominant mechanism driving the softening has largely been hampered by a lack of sufficient observations while the X-ray spectrum is actively softening. Part of the reason is that the timing of such observations is difficult. Also, the low-luminosity nature of BH-LMXBs during the transition to quiescence prevents precise measures of the X-ray spectral shape for all but the closest BH-LMXBs with low line-of-sight absorption. Furthermore, from X-ray observations alone, it is extremely challenging to differentiate between the scenarios described above.

One can make meaningful progress, however, by performing high signal-to-noise ratio X-ray spectral monitoring in coordination with radio observations. As hard-state BH-LMXBs transition toward quiescence, they trace out distinct paths through the $L_{\text{R}}\text{--}L_{\text{X}}$ plane, where L_{R} is the radio luminosity (e.g., Corbel et al. 2013; Gallo et al. 2014, 2018). The presence of correlated radio and X-ray emission suggests a link between the innermost regions of the accretion flow/jet (probed by X-rays) and the outer regions of the jet (probed by radio observations). So far, three BH-LMXBs have been seen to follow a similar nonlinear correlation of the form $L_{\text{R}} \propto L_{\text{X}}^{0.5\text{--}0.7}$ (Gallo et al. 2014), which is often referred to as the “standard track.” In addition, the only three highly sub-Eddington ($L_{\text{X}} \sim 10^{-8.5} L_{\text{Edd}}$) BH systems with meaningful radio constraints lie on the extrapolation of the standard track (Gallo et al. 2006, 2014; Corbel et al. 2013; Dzib et al. 2015; Ribó et al. 2017;

¹² Note that, at the very lowest accretion rates, one expects the X-ray spectrum to be dominated by bremsstrahlung radiation in most RIAF models (e.g., Yuan & Narayan 2014).

Tremou et al. 2020). However, a large population of hard-state BH-LMXBs that are “radio faint” compared to the standard track also exists (see, e.g., Corbel et al. 2004; Xue & Cui 2007; Gallo et al. 2012). Under certain assumptions, the slope of the $L_{\text{R}}\text{--}L_{\text{X}}$ correlation can be used to place constraints on the emission mechanisms at work (see also Markoff et al. 2003; Heinz & Sunyaev 2003), such that combining X-ray (spectroscopy) with radio monitoring has the potential to break model degeneracies (see, e.g., high-cadence radio/X-ray monitoring of the 2015 decay of V404 Cygni; Plotkin et al. 2017b).

In this work, we present radio and X-ray observations of the BH-LMXB MAXI J1820+070 during the decay of its initial outburst in 2018 and of one of the subsequent reflares that occurred in 2019. In Section 2 we introduce the source, before detailing our observations and data reduction in Section 3. We present and discuss our results in Section 4 and summarize in Section 5. Throughout this work, we adopt a distance of $d = 2.96 \pm 0.33$ kpc, as determined from trigonometric parallax in the radio wave band by Atri et al. (2020) using very long baseline interferometry.

2. MAXI J1820+070

MAXI J1820+070 (also known as ASASSN-18ey; Tucker et al. 2018) was discovered as an optical transient in 2018 March by the All-Sky Automated Survey for SuperNovae (ASAS-SN; see Shappee et al. 2014; Kochanek et al. 2017). Six days after the initial optical detection, the Monitor of All-Sky X-ray Image (MAXI; Matsuoka et al. 2009) reported a bright X-ray transient associated with the optical source (Denisenko 2018; Kawamuro et al. 2018). Follow-up observations were performed across the electromagnetic spectrum (e.g., Baglio et al. 2018; Bright et al. 2018; Uttley et al. 2018) and hinted at a potential BH-LMXB nature for the source. The compact object was dynamically confirmed as a $>5.18 \pm 0.15 M_{\odot}$ BH by Torres et al. (2019), later refined to $M_{\text{BH}} = 8.48^{+0.79}_{-0.72} M_{\odot}$ (Torres et al. 2020).¹³ The binary orbital period, P_{orb} , of MAXI J1820+070 is 16.5 hr (Torres et al. 2019).

The initial outburst lasted for almost a year¹⁴ and approached quiescence in 2019 February (Russell et al. 2019). However, the source underwent two reflares (see Zhang et al. 2019 for the classification scheme of BH-LMXB rebrightening episodes), which lasted ~ 2 months each, in 2019 March (Ulowetz et al. 2019) and August (Hamsch et al. 2019), as well as a third, shorter reflare in 2020 February (Adachi et al. 2020).

The brightness of MAXI J1820+070 ($L_{\text{X}} \sim 0.15 L_{\text{Edd}}$ at peak; Atri et al. 2020) during its outburst has made it an exciting candidate for studies of accretion and outflow in BH-LMXBs. For example, “reverberation lags,” lags between the corona and the irradiated accretion disk, showed, for the first time, evidence for a contracting corona in a BH-LMXB (Kara et al. 2019). During the hard-to-soft state transition of the main outburst, MAXI J1820+070 launched long-lived bipolar radio and X-ray ejecta that imply jet powers far larger than inferred from radio flares during the soft-state transition (Bright et al. 2020; Homan et al. 2020; Espinasse et al. 2020). Finally, observations of MAXI J1820+070 during the soft state revealed an excess emission component in the X-ray spectrum,

¹³ Assuming the binary inclination is equivalent to the inclination of the radio jet ($63^{\circ} \pm 3^{\circ}$; Atri et al. 2020).

¹⁴ See the MAXI light curve: http://maxi.riken.jp/star_data/J1820+071/J1820+071_00055058g_lc_all.gif.

which has been interpreted as originating in the “plunge” region, where matter begins to fall freely into the BH (Fabian et al. 2020). Contrary to many of the studies discussed above, the work we present here focuses on the source as it approaches quiescence, in an effort to constrain the emission mechanisms at work in BH-LMXBs at low luminosities.

3. Observations and Analysis

Observations were assembled through multiple target of opportunity (ToO) programs designed to piece together dense multiwavelength spectral monitoring of the entire hard-state decay of a transient black hole. For the beginning of the decay ($L_X \approx 10^{-2}$ to $10^{-4} L_{\text{Edd}}$), covering MJD 58397–58519, MAXI J1820+070 was monitored with the X-ray Telescope (XRT) on board the Neil Gehrels Swift Observatory (Burrows et al. 2005). In this work, we use data from a combination of guaranteed time observations (GTOs; PI Gallo) and regular ToOs, obtaining a total of 21 observations during the decay of the initial outburst, with an average cadence of ~ 2 days. Each GTO Swift epoch was coordinated within ± 1 day of a radio observation taken with the Karl G. Jansky Very Large Array (VLA) through program 18A-277 (PI Plotkin). We then triggered a joint Chandra/VLA proposal to monitor the source at lower luminosities (Chandra proposal ID 19400238; PI Gallo). However, we were only able to obtain a single epoch on MJD 58441 before the source became Sun-constrained (although we note that we did continue to monitor in the radio during the X-ray Sun constraint, albeit less frequently). Prior to and following the Sun constraint, MAXI J1820+070 was also observed three times through a joint Chandra/VLA program on MJD 58436 and 58518–58519 (Chandra proposal ID 19400337; PI Corbel; see Espinasse et al. 2020). Finally, after the detection of the first reflare, we triggered another joint Chandra/VLA program to observe its decay six times at low luminosities ($L_X \lesssim 10^{-4} L_{\text{Edd}}$), typically every ~ 9 days from MJD 58603 to 58645 (Chandra proposal ID 20400114; PI Gallo).

For completeness, we also include all Swift/XRT observations available in the archive during the decay of the first reflare (covering MJD 58563–58591), and we also include two observations with the X-ray Timing Instrument on the Neutron star Interior Composition Explorer (NICER/XTI; Gendreau et al. 2016) close to the end of the main outburst coverage. A summary of all X-ray and radio observations utilized in this work is presented in Tables A1 and A2 in the Appendix.

3.1. Swift/XRT

MAXI J1820+070 was monitored regularly by Swift since its initial discovery. In this work, we use a subset of the observations spanning the date range 2018 October 6 to 2019 April 17 (MJD 58397–58590; Target ID: 10627), covering the decline of the initial outburst of the source and the decline of the first reflare. Swift/XRT operated in windowed timing (WT) mode for all of the observations we analyze in this work. All photon counting (PC) mode observations had count rates that were either too high (such that photon pileup was too great to correct for) or too low (such that not enough photons were collected to construct a spectrum with good signal-to-noise ratio).

Data were reprocessed using the `xrtpipeline` tool, part of the HEASOFT v6.26.1 software suite for analysis of

high-energy astrophysical data.¹⁵ Spectral products were extracted using the `xrtproducts` tool. Source counts were extracted from a circular region 20 pixels ($\approx 47''$) in radius, centered on the source. Background counts were extracted from an annulus centered on the source, with inner and outer radii 80 and 120 pixels, respectively. Response matrices were generated using version 20191017 of the calibration database (CALDB).

Individual spectra were grouped such that each spectral bin contained a minimum of 15 counts. Spectral fits were performed with XSPEC v12.10.1f (Arnaud 1996), using Cash statistics modified for background-subtracted spectra (W-statistic; Cash 1979) as the fitting statistic, which is appropriate for fitting low-count spectra while also tending to χ^2 in the high-count regime. The majority of spectra were well fit with an absorbed power-law model (`powerlaw` in XSPEC), with interstellar absorption accounted for by the `tbabs` model (Wilms et al. 2000). The first three Swift spectra (MJD 58397–58402) were statistically improved with the addition of a disk blackbody model (`diskbb`) with an inner disk temperature in the range $kT_{\text{in}} = 0.13$ –0.18 keV. The presence of the disk component was confirmed by a NICER observation on MJD 58400.9. When including a `diskbb` component for spectral fits at $\text{MJD} > 58402$, we found the disk normalization was consistent with zero. We extracted unabsorbed 1–10 keV fluxes using the `cflux` model. Uncertainties on the best-fit X-ray parameters are all 90% confidence unless otherwise stated.

The first 10 Swift observations of our campaign ($\text{MJD} < 58420$) were taken primarily through our GTO program, where we compensated for the decrease in flux with time by increasing the length of each subsequent Swift/XRT exposure. In turn, we obtained a relatively steady number of X-ray counts in each spectrum. Later in the decay when MAXI J1820+070 was even fainter, all Swift exposures were relatively short, making it difficult for us to assess degeneracies between best-fit column densities (N_{H}) and photon indices (Γ). Since a primary goal of our program is to quantify changes in X-ray spectral shape, and since we do not expect N_{H} to evolve during the decay, we chose to freeze N_{H} to $1.0 \times 10^{21} \text{ cm}^{-2}$ throughout our entire campaign to allow a more uniform comparison between the higher- and lower-count spectra toward the beginning and end of our campaign, respectively. This value is (a) consistent with the Galactic column in the direction of MAXI J1820+070 (HI4PI Collaboration et al. 2016) and (b) consistent with the measured values of N_{H} over the course of its outburst (see, e.g., Shidatsu et al. 2018; Kajava et al. 2019; Xu et al. 2020). In addition, during the first 10 Swift observations, where we accounted for the diminishing count rate through increased exposure times, we find a weighted-average $N_{\text{H}} = (1.1 \pm 0.1) \times 10^{21} \text{ cm}^{-2}$ if we allow N_{H} to be free.

3.2. Chandra/ACIS

We utilized Chandra observations of MAXI J1820+070 over the date range 2018 November 13 to 2019 June 11 (MJD 58435–58645), which includes observations during the decline of the initial outburst as well as the final stages of the decline of the first reflare. For all observations, the source was placed at the aim point of the S3 chip on the Advanced CCD Imaging Spectrometer (ACIS; Garmire et al. 2003). Three observations employed the High-Energy Transmission Grating (HETG; Canizares et al. 2005) as a filter in order to avoid photon pileup. Data were reduced using CIAO (Chandra Interactive Analysis

¹⁵ <https://heasarc.gsfc.nasa.gov/docs/software/heasoft/>

of Observations) v4.11 and the Chandra CALDB v 4.8.4.1 (Fruscione et al. 2006). We reprocessed the data using the `chandra_repro` script to apply the latest calibrations and bad pixel files. Spectral products were extracted using the `specextract` script for the majority of the observations. For each of these, source counts were extracted from a circle of radius $2''$ centered on the source, while we extracted the background from an annular region centered on the source with inner and outer radii $9''$ and $20''$, respectively.¹⁶ One observation (ObsID 20207) without the HETG in place suffered from extreme photon pileup, for which we were unable to effectively correct. In this case, we extracted a spectrum from the CCD readout streak that appears in bright observations such as this one.¹⁷ Source counts were extracted using two box regions of size $2'' \times 51''$ centered on each streak on either side of the piled-up point source, and background counts from two box regions of size $22'' \times 51''$ at the same location (with the source region excluded). Spectra were extracted with the CIAO tool `dmlextract`, and response files were created using `mkacisrmf` and `mkarf`. The effective exposure time of the readout streak spectrum was 296 s.

As with the Swift data, we used XSPEC to perform spectral fitting. For the shorter Chandra observations (exposure time $t_{\text{exp}} < 10$ ks), we chose to bin the spectra such that each bin contained a minimum of one count. For the remaining, longer observations, we grouped the spectra to a minimum of 15 counts per spectral bin, as with the Swift spectral fits. All Chandra spectra were well fit with an absorbed power-law model and were not statistically improved with the addition of a `diskbb` model. Unabsorbed 1–10 keV fluxes were extracted in the same way as for the Swift data.

3.3. NICER

NICER observed MAXI J1820+070 regularly since its initial discovery. In this work, we utilize two observations from 2018 November 19 and 21 (MJD 58441 and 58443; ObsIDs 1200120310 and 1200120312; PI Gendreau) covering the initial decline immediately after the Swift and Chandra coverage ended. Both observations were recalibrated with the `nicer12` task in HEASOFT v6.26.1, using CALDB version 20200202. Spectra were extracted from all active detectors, except detectors #14 and #34, which are prone to excessive noise. Background spectra were created using the “3C50_RGv5” model provided by the NICER team. We used response files recommended for CALDB version 20200202.

We followed the same spectral fitting procedure as for the Swift data, grouping the data such that each bin contained a minimum of 25 counts and utilizing the Cash (1979) fitting statistic. Spectra were fit in the 0.5–10 keV range, and we included a multiplicative constant of 50/52 in the model to account for the excluded detectors. Both NICER spectra were well fit with an absorbed power-law model.

3.4. VLA

Our VLA campaign consisted of 19 observations obtained through NRAO programs 18A-277, SK0335, SJ0238, and SK0114; see Table A2. The first eight VLA observations (MJD 58398–58432) were taken in the most compact D

configuration (maximum baseline $B_{\max} = 1.03$ km), with the next five observations (MJD 58441–58517) in C configuration ($B_{\max} = 3.4$ km), and the final six observations (MJD 58603–58645; during the reflare decay) in B configuration ($B_{\max} = 11.1$ km). Observations lasted between ~ 30 and 120 minutes (providing ~ 1 –80 minutes on source), with longer observations generally toward the end of each decay.

All data were taken in the C-band (4–8 GHz) with 4 GHz total bandwidth (2×2 GHz basebands centered at 5.0 and 7.0 GHz). For every observation, we used scans on 3C 286 for bandpass calibration and to set the flux density scale (using the Perley & Butler 2017 coefficients), and we interleaved our science observations with scans on the secondary calibrator J1824+1044 to solve for time-dependent complex gain solutions. Data were reduced using the Common Astronomy Software Application v5.6 (CASA; McMullin et al. 2007), and calibrations were performed using the VLA pipeline. A small amount of additional flagging was performed manually prior to imaging the data.

The data were imaged using `tclean`, using two Taylor terms to model spectral dependences of sources within the field. We used Briggs weighting to reduce sidelobes from other sources in the field, using robust values of 0.0, 0.5, and 1.0 when the array was in D, C, and B configurations, respectively. During the first nine observations, MAXI J1820+070 was >1 mJy, and we performed one to two rounds of phase-only self-calibration (down to 30–60 s solution intervals). We achieved rms noise levels ranging from ≈ 3 to ≈ 50 μJy bm^{-1} across our entire campaign, as measured from source-free regions of our radio images. All flux densities were measured at 6 GHz.

Long-lived ejecta that were launched by MAXI J1820+070 during its soft state transition (see Section 2) were present during our coverage of the initial decay. During our D-configuration observations, we found it challenging to resolve the core from these ejecta in the image plane, which reached distances up to $13''$ from the compact core. We therefore measured flux densities by fitting the blended core and ejecta in the uv plane using `uvmultifit`¹⁸ (Martí-Vidal et al. 2014), as described below.

For each D-configuration observation, we first produced an image in `tclean`, as described above. We then took the sky model produced by `tclean`, masked out the MAXI J1820+070 complex, and subtracted remaining “field” sources from the visibility set using the task `uvsub`. Depending on the date of observation and the time on source, we expected to detect anywhere from zero to two relativistic ejecta in each observation in addition to the compact core. We therefore ran three iterations of `uvmultifit`, requiring one, two, and three point sources. For the core, we left the radio spectral index α ($f_{\nu} \propto \nu^{\alpha}$, where f_{ν} is the flux density at frequency ν) as a free parameter, and for the relativistic ejecta we fixed the spectral index to $\alpha = -0.7$ (Bright et al. 2020). We examined the resulting fit statistics to guide our decision on the best fit (i.e., the one-, two-, or three-component model); we also examined residual images after subtracting each model (i.e., we used `uvsub` to subtract each model from the visibility set and then created “dirty images” using `tclean`). The peak flux densities and spectral indices of only the core (from our preferred model) are reported in Table A2. Uncertainties incorporate both rms

¹⁶ We note that the background region did not include the X-ray jets presented by Espinasse et al. (2020).

¹⁷ <https://cxc.cfa.harvard.edu/ciao/threads/streakextract/>

¹⁸ <https://github.com/onsala-space-observatory/UVMultiFit>

noise and errors related to the fitting process. Flux densities (and positions) for the relativistic ejecta were reported in Bright et al. (2020).

When the VLA was in its C configuration, we could resolve the compact core from the ejecta in the image plane. We generally found for these observations, when the core was fainter, that flux density measurements appeared more reliable in the image plane compared to the uv plane. We therefore measured the peak flux density of the compact core using the task `imfit` for our C-configuration observations, but using a model that required one, two, or three point-source components. As above, we examined residual images with each model subtracted to decide on the number of required components. The flux densities reported in Table A2 (for our C-configuration observations) are the peak flux densities reported by `imfit` only for the core. All of our B-configuration observations are during the reflare decay, by which time radio emission from the relativistic ejecta had completely faded.

For the C- and B-configuration observations, we measured radio spectral indices by splitting our bandwidth into 4×1 GHz basebands centered at 4.5, 5.5, 6.5, and 7.5 GHz. We then imaged each baseband separately and measured the flux density of the core in `imfit` (using multicomponent models in C configuration, as described above). The spectral index was then measured by performing a least-squares fit, with the uncertainty on α estimated by Monte Carlo simulations that randomized (and refit) each spectrum (see Plotkin et al. 2017b). Note that for the D-configuration observations, the spectral index was fit as a free parameter when running `uvmultifit`. Throughout the text, we adopt radio luminosities at 5 GHz as calculated from the measured radio flux density (at 6 GHz), the radio spectral index, and the source distance.

4. Results and Discussion

4.1. X-Ray Luminosity and Spectral Evolution

The X-ray light curve of MAXI J1820+070 is shown in the upper panel of Figure 1, highlighting the end of the initial outburst and the decay of the first reflare in 2019 March. We incorporate the uncertainty on the distance into our luminosity calculation. The decline of both the initial outburst and the first reflare cover a similar dynamic range in Figure 1, with each covering ~ 3 orders of magnitude in L_X . It is unclear if MAXI J1820+070 reached its minimum quiescent L_X between the end of the initial outburst and the onset of the first reflare, because X-ray observations of the source at an L_X lower than that measured by our final Chandra epoch do not exist at the time of writing. However, considering the P_{orb} of MAXI J1820+070, we suspect that it may eventually settle to an L_X up to 1–2 orders magnitude lower than the minimum observed during our campaign (see, e.g., Figure 4 of Reynolds & Miller 2011).

The lower panel of Figure 1 shows the evolution of the X-ray spectrum, parameterized by the photon index Γ . The hard X-ray spectrum ($\Gamma \lesssim 1.7$), coupled with the presence of a compact jet, indicates that MAXI J1820+070 had transitioned to the hard state by the time we commenced our $L_R - L_X$ monitoring program. This is confirmed by the detection of significant variability (fractional rms $\gtrsim 35\%$) and quasi-periodic oscillations in the Swift and NICER light curves (Stiele & Kong 2020), typical of BH-LMXBs in the hard state.

We see a mild hardening of the X-ray spectrum of MAXI J1820+070 for the first ≈ 15 days of our program, with Γ

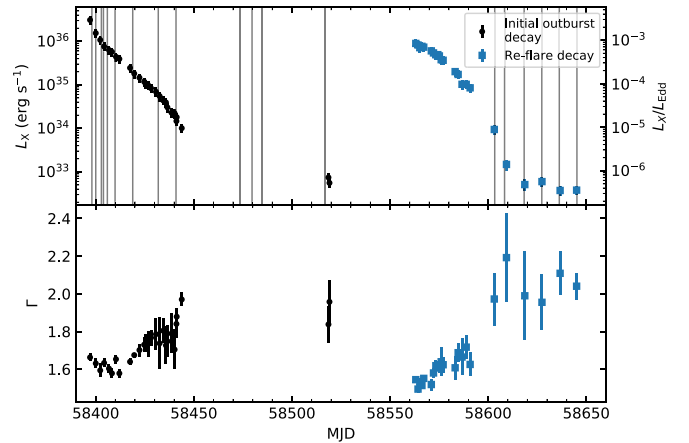


Figure 1. Upper panel: 1–10 keV X-ray light curve of MAXI J1820+070. The gray vertical lines represent the epochs of the VLA observations. Luminosities were calculated by adopting the distance $d = 2.96 \pm 0.33$ kpc as measured by Atri et al. (2020). For the Eddington ratios labeled on the right y-axis, L_{Edd} is calculated assuming the mass of the BH $M_{\text{BH}} = 8.48 M_{\odot}$ as derived by Torres et al. (2020). Plotted L_X is unabsorbed. Lower panel: best-fit value of the power-law index (Γ) for each observation. In both panels, black, circular points represent observations of the decay of the initial outburst, and blue, square points represent observations taken during the decay of the first reflare.

evolving from ≈ 1.7 to 1.6 (reaching its hardest values as the source declined from $L_X \approx 10^{36.5}$ to $10^{35.6}$ erg s^{-1} , equivalent to $\approx 10^{-2.5}$ to $10^{-3.4} L_{\text{Edd}}$). During the first three observations (MJD 58397–58402), we detect a cool, thin disk ($kT = 0.13$ – 0.18 keV) in the hard state that slowly fades and is not detectable at later epochs with lower-count spectra ($L_X \lesssim 10^{-3} L_{\text{Edd}}$). An accretion disk component is not uncommon in the spectra of BH-LMXBs in the canonical hard state, particularly at these modest Eddington ratios (e.g., Miller et al. 2006; Reis et al. 2010; Reynolds & Miller 2013). During the decline of the second reflare of MAXI J1820+070, Xu et al. (2020) found strong evidence for a truncated disk at $L_X \approx 10^{-2.6} L_{\text{Edd}}$, similar to the luminosity at which we require a disk component in the spectra during the decline of the main outburst.

At lower X-ray luminosities during the initial decay, we observe Γ evolve from ~ 1.6 to 2.0. The initial hardening and then softening of Γ with decreasing X-ray luminosity is a well-known trend (one suggestion is that it is driven by a change in the source of seed photons for inverse Comptonization; see, e.g., Sobolewska et al. 2011; Kajava et al. 2016). Based on two Chandra observations taken on MJD 58519, the X-ray spectrum did not appear to continue to soften indefinitely. Unfortunately, we cannot empirically confirm this statement, since we lack X-ray coverage for MJDs 58444–58519 because the source was too close to the Sun for X-ray observations. Nevertheless, even though we cannot determine exactly when the X-ray spectrum “saturated” to its maximum Γ during the initial decay, we can place a limit that Γ saturated on or after MJD 58444, when $L_X \approx 10^{34}$ erg s^{-1} ($\approx 10^{-5} L_{\text{Edd}}$).

Our coverage of the decay of the reflare started 1–2 days after its peak, in contrast with the observations of the decline of the initial outburst, which we commenced ~ 200 days postpeak, after the source had undergone state transitions. During the decay of the reflare, we only observed the stage of the decay when Γ increases. Here, it is more apparent that once $\Gamma \approx 2$ was reached, the X-ray spectrum plateaued to that value, which occurred sometime between the last Swift observation and the first Chandra observation during the reflare (58591 $<$ MJD $<$ 58603,

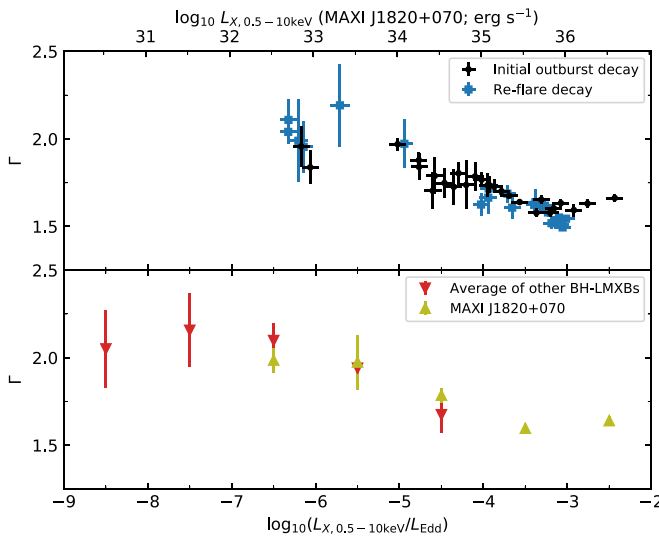


Figure 2. X-ray spectral evolution of MAXI J1820+070 as a function of Eddington fraction. Upper panel: unbinned data from Figure 1, with the same legend. Lower panel: the same data, in Eddington fraction bins of width 1 dex (yellow triangles), plotted alongside the photon indices of 10 BH-LMXBs collected by Plotkin et al. (2013), with additional data from V404 Cygni included since its 2015 outburst (Plotkin et al. 2017b), again in Eddington fraction bins of 1 dex (red inverted triangles). Plotted luminosities for all sources are in the 0.5–10 keV energy band.

$10^{-4} \gtrsim L_X/L_{\text{Edd}} \gtrsim 10^{-5}$). The X-ray spectrum then remains soft ($\Gamma \approx 2$) over >1.5 decades in X-ray luminosity ($10^{-5} \gtrsim L_X/L_{\text{Edd}} \gtrsim 10^{-6.4}$).

4.1.1. Comparisons to Other Quiescent Sources

In Figure 2 we show Γ as a function of Eddington fraction for both the initial decay and reflare. This figure demonstrates the softening of the X-ray spectrum (i.e., increasing Γ) as X-ray luminosity decreases, with Γ eventually “saturating” to ≈ 2 at $L_X \approx 10^{-5} L_{\text{Edd}}$. The bottom panel of Figure 2 shows the X-ray spectrum binned by X-ray luminosity, to ease comparisons to the ensemble average of other BH-LMXBs in the Chandra archive from Plotkin et al. (2013), combined with additional data from V404 Cygni (Plotkin et al. 2017b).¹⁹ Among all of the quiescent BH-LMXBs in the Chandra archive, the only individual source (besides MAXI J1820+070) where the X-ray softening has been tracked through the “plateau” stage is V404 Cygni (during its 2015 outburst decay; Plotkin et al. 2017b).²⁰ For V404 Cygni, the softening proceeded quickly (on a timescale of <3 days) and saturated at a slightly lower luminosity $L_X \approx 10^{-5.5}–10^{-5.6} L_{\text{Edd}}$.

Comparing MAXI J1820+070, V404 Cygni, and the ensemble of other quiescent BH-LMXBs, we are starting to uncover potential variations in the X-ray softening between different sources. The general qualitative trend—that the softening completes below $\approx 10^{-5} L_{\text{Edd}}$ and then plateaus—holds. However, the softening appears to occur gradually in MAXI J1820+070, at least according to the initial decay where Γ increased over ~ 30 days (we do not have sufficient coverage during the reflare decay; see Figure 1). Conversely, the active X-ray softening of V404 Cygni was much

¹⁹ It is also for this ease of comparison that we utilize 0.5–10 keV luminosities of MAXI J1820+070 in this figure instead of the 1–10 keV luminosities quoted throughout this work.

²⁰ Though the intermediate-mass X-ray binary 4U 1543–47 has good coverage of the plateau phase with the Rossi X-ray Timing Explorer (Kalemci et al. 2005).

more rapid, occurring over <3 days (Plotkin et al. 2017b). Considering the strong relation between L_X and Γ , this softening timescale can be considered to be a proxy for the timescale of the luminosity decay.

Besides MAXI J1820+070 and V404 Cygni, we identify one other source in the literature with comparable coverage of the X-ray softening and plateau of Γ : 4U 1543–47, which softened from $\Gamma \approx 1.6$ to 2.0 over ~ 5 days and then plateaued during the decay of its 2002 outburst (Kalemci et al. 2005). Another BH-LMXB, Swift J1357.2–0933, also has excellent spectral constraints of the X-ray softening during its 2011 and 2017 decays, which took ~ 90 days (Armas Padilla et al. 2013; Beri et al. 2019), but became too faint to obtain useful constraints during the plateau stage. Considering the ensemble of these four systems, BH transitions into quiescence appear to fall into categories with gradual softenings (i.e., MAXI J1820+070 and Swift J1357.2–0933) and fast softenings (i.e., V404 Cygni and 4U 1543–47). One might be tempted to link the softening timescale to the P_{orb} of the system (and therefore the disk size for Roche Lobe overflow systems), since Swift J1357.2–0933 with the slowest softening (~ 90 days) has the shortest orbital period ($P_{\text{orb}} = 2.8$ hr; Corral-Santana et al. 2013) and V404 Cygni with the fastest softening (<3 days) has the longest orbital period ($P_{\text{orb}} = 6.5$ days; Casares et al. 1992), with MAXI J1820+070 ($P_{\text{orb}} = 16.5$ hr; Torres et al. 2019) and 4U 1543–47 ($P_{\text{orb}} = 1.1$ days; Orosz et al. 1998) falling in between. Nevertheless, the apparent differences in the softening timescales between these four systems further highlight the need for improved X-ray spectral coverage during decays of systems spanning a wide range of properties like P_{orb} , inclination, and donor mass, in order to attach a physical scenario to the timescale of the transition into quiescence.

4.2. Radio Luminosity and Spectral Evolution

In the upper panel of Figure 3, we show the 5 GHz radio light curve of the compact core of MAXI J1820+070, and we show the time evolution of the radio spectral index α in the lower panel. The radio spectrum is inverted in nearly all of our observations (typically $\alpha > 0.2$; the weighted-average spectral index is $\bar{\alpha} = 0.24 \pm 0.06$, where the quoted uncertainty represents the standard deviation about the weighted average).

We see some variations in α with time. To investigate a potential correlation between $\log_{10} L_R$ and α , we calculate the Spearman correlation coefficient, ρ , and incorporate the uncertainties on the input parameters by simulating 10,000 data sets based on the original sample, allowing L_R and α to vary within their error bars according to a (log)normal distribution. We find $\rho = -0.2 \pm 0.2$, where this value represents the median of the 10,000 values of ρ calculated from the simulated data, and the 1σ uncertainties are calculated as the 16th and 84th percentiles. The value of ρ is consistent with no correlation between α and $\log_{10} L_R$. To test the significance, we adopt a Monte Carlo method by randomly shuffling the data, creating 10,000 new $\log_{10} L_R$, α pairs and calculating ρ each time. We find that 17% of the time we measure an anticorrelation that is as strong as, or stronger than, $\rho = -0.2$, implying that our measured value of ρ is not significant.

Perhaps the most interesting variation in α occurs on MJD 58603, where α veers slightly negative ($\alpha = -0.11 \pm 0.04$), and possibly also on MJDs 58485 and 58517 (at much lower statistical significance). Such negative deviations, however, are

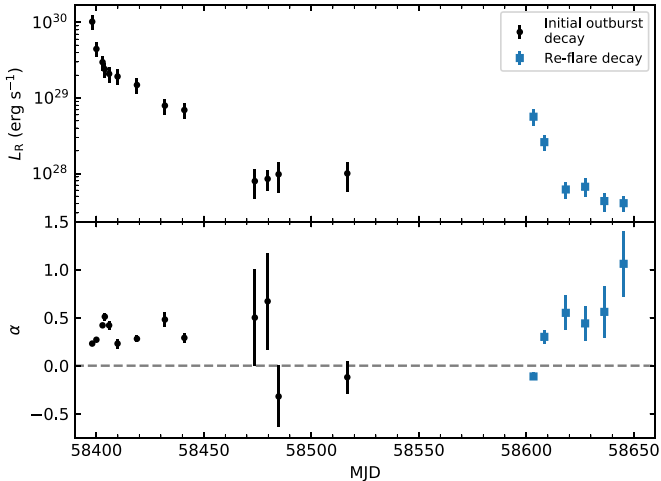


Figure 3. Upper panel: 5 GHz radio light curve of MAXI J1820+070. Luminosities were calculated by adopting the distance $d = 2.96 \pm 0.33$ kpc as measured by Atri et al. (2020). Lower panel: best-fit value of the radio spectral index (α) for each observation. The horizontal dashed line represents a value of $\alpha = 0$, that is, a flat spectrum. In both panels, black, circular points represent observations of the decay of the initial outburst, and blue, square points represent observations taken during the decay of the first reflare.

not exceptional and do not approach becoming optically thin (where typically $\alpha \approx -0.7$), and similarly, mild negative deviations in α have been observed for other low-luminosity hard-state and quiescent BH-LMXBs (e.g., Rana et al. 2016; Espinasse & Fender 2018; Plotkin et al. 2019). A slightly negative value of α such as the instances discussed here could perhaps indicate the jet break temporarily moving below gigahertz radio frequencies. Alternatively, we may be seeing deviations from a simple conical jet, or we may be seeing an optically thin emission region (perhaps related to a small flare) superposed over a flat/inverted radio spectrum from the compact jet.

4.3. Radio–X-Ray Correlation

Figure 4 shows MAXI J1820+070 in the L_R – L_X plane. The parameters L_R and L_X , along with their corresponding spectral indices, are also tabulated in Table 1. MAXI J1820+070 displays a nonlinear correlation over ≈ 4 decades in X-ray luminosity extending from the hard state through quiescence. To measure the slope of the correlation, we adopt the Bayesian modeling package linmix,²¹ the PYTHON port of the LINMIX_ERR IDL package (Kelly 2007), to measure the dependence of L_R on L_X . We assume a linear correlation of the form $\ell_R = b + m\ell_X$, where ℓ_R and ℓ_X are the logarithms of L_R and L_X , respectively, and b and m are the ℓ_R -intercept and slope, respectively. Following Gallo et al. (2012, 2014, 2018), we include additional uncertainties of 0.3 dex on ℓ_R and ℓ_X to account for the lack of strict simultaneity between our radio and X-ray observations. MAXI J1820+070 follows a relation with slope $m = 0.52 \pm 0.07$, with an intrinsic random scatter $\sigma_0 = 0.14_{-0.07}^{+0.10}$ dex, where the best-fit values represent the median of 10,000 draws from the posterior distributions and the 1σ uncertainties are calculated as the 16th and 84th percentiles. The correlation slope is consistent with that derived for the larger hard-state BH population ($m = 0.59 \pm 0.02$ from 36 BHs; Gallo et al. 2018).

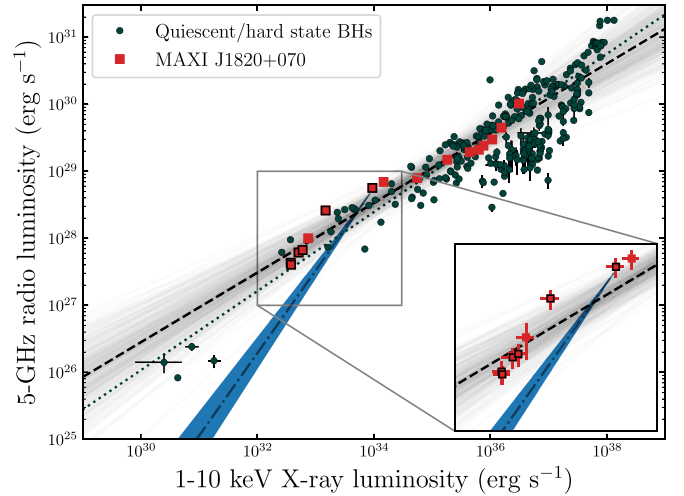


Figure 4. MAXI J1820+070 on the radio–X-ray plane (red squares). Observations taken during the decay of the first reflare are highlighted with black boxes. Also plotted for comparison are a sample of quiescent/hard-state BH-LMXBs (dark green circles). The dashed line shows the best-fit $L_R \propto L_X^{0.52}$ correlation to the MAXI J1820+070 data. For clarity, in the main panel we do not plot the uncertainties on the MAXI J1820+070 luminosities, but they are taken into account during the fitting process. The gray solid lines show some samples from the posterior distribution of best fits to the correlation. The dotted line shows the best-fit $L_R \propto L_X^{0.59}$ correlation for a sample of 36 BHs from Gallo et al. (2018), highlighting the “standard track.” The dotted-dashed line indicates the predicted path that MAXI J1820+070 would take through the radio–X-ray plane if the observed spectral softening (which completes at $L_X \approx 10^{34}$ erg s $^{-1}$) was due to a switch to synchrotron-cooled X-ray emission, with the blue shaded region representing the expected scatter about the line. We show a zoomed-in region of the lowest luminosity points in the inset, with error bars on the data. Data for the quiescent/hard-state BHs were obtained from A. Bahramian’s Radio/X-ray correlation database for X-ray binaries (Bahramian et al. 2018).

MAXI J1820+070 is only the fourth individual source for which an unbroken L_R – L_X correlation has been tracked over four (or more) decades in X-ray luminosity, joining V404 Cygni ($m = 0.54 \pm 0.03$; Corbel et al. 2008; Plotkin et al. 2017b), GX 339–4 ($m = 0.62 \pm 0.01$; Corbel et al. 2013; see also Tremou et al. 2020), and XTE J1118+480 ($m = 0.72 \pm 0.09$; Gallo et al. 2014). Note that we are aware of two other sources with L_R – L_X coverage over a comparable range of luminosities, H1743–322 and Swift J1753.5–0127; however, both sources appear to follow different correlation slopes above and below $L_X \approx 10^{34}$ erg s $^{-1}$ (Coriat et al. 2011; Plotkin et al. 2017a), such that we do not compare MAXI J1820+070 to those two sources here. MAXI J1820+070 also shows the same L_R – L_X correlation over multiple decays, similar to V404 Cygni (Plotkin et al. 2017b) and GX 339–4 (Corbel et al. 2013). This suggests that the coupling between the disk and the jet is robust between outburst decays.

We can combine the slope of the L_R – L_X correlation with radio spectral information to draw some conclusions about the dominant emission mechanisms at work as the source decays. If the radio luminosity is responding to changes in the mass accretion rate (\dot{M}), then $L_R \propto \dot{M}^{17/12 - 2/3\alpha}$ (Heinz & Sunyaev 2003; Markoff et al. 2003).²² The above assumes that jets are emitting synchrotron radiation from nonthermal particles accelerated into a power-law distribution, $dn/d\gamma \propto \gamma^{-p}$ (where n is the number density of particles, γ is the Lorentz factor, and p is the

²¹ <https://linmix.readthedocs.io/en/latest/>

²² Heinz & Sunyaev (2003) define $f_\nu \propto \nu^{-\alpha}$, so the formulae in this work differ by a minus sign.

Table 1
Summary of Results from the Quasi-simultaneous X-Ray and Radio Observations

MJD _X (1)	$\log_{10} L_X(1\text{-}10 \text{ keV})^{\text{a}}$ (erg s ⁻¹) (2)	Γ (3)	MJD _R (4)	$\log_{10} L_R(5 \text{ GHz})$ (erg s ⁻¹) (5)	α (6)
58397.09	36.5 ± 0.1	1.66 ± 0.02	58398.04	30.0 ± 0.1	0.23 ± 0.00
58400.01	36.2 ± 0.1	1.63 ± 0.03	58399.99	29.6 ± 0.1	0.27 ± 0.01
58402.28	36.0 ± 0.1	1.59 ± 0.04	58402.85	29.5 ± 0.1	0.42 ± 0.02
58404.26	35.9 ± 0.1	1.63 ± 0.02	58403.91	29.4 ± 0.1	0.51 ± 0.04
58406.73	35.8 ± 0.1	1.60 ± 0.02	58405.90	29.3 ± 0.1	0.42 ± 0.05
58410.30	35.6 ± 0.1	1.65 ± 0.02	58409.83	29.3 ± 0.1	0.23 ± 0.05
58419.61	35.3 ± 0.1	1.67 ± 0.01	58418.85	29.2 ± 0.1	0.28 ± 0.03
58432.55	34.7 ± 0.1	1.74 ± 0.14	58431.85	28.9 ± 0.1	0.48 ± 0.07
58441.11	34.2 ± 0.1	1.84 ± 0.07	58440.90	28.8 ± 0.1	0.29 ± 0.05
58518.61	32.9 ± 0.1	1.84 ± 0.10	58516.70	28.0 ± 0.2	-0.12 ± 0.17
58603.13	34.0 ± 0.1	1.97 ± 0.14	58603.32	28.8 ± 0.1	-0.11 ± 0.04
58609.33	33.2 ± 0.1	2.19 ± 0.23	58608.35	28.4 ± 0.1	0.30 ± 0.07
58618.67	32.7 ± 0.1	$1.99^{+0.24}_{-0.23}$	58618.34	27.8 ± 0.1	0.55 ± 0.18
58627.42	32.8 ± 0.1	1.95 ± 0.15	58627.34	27.8 ± 0.1	0.44 ± 0.18
58636.67	32.6 ± 0.1	2.11 ± 0.12	58636.26	27.6 ± 0.1	0.56 ± 0.27
58645.08	32.6 ± 0.1	2.04 ± 0.07	58645.24	27.6 ± 0.1	1.06 ± 0.34

Note.

^a Unabsorbed.

power-law index that describes the energy distribution of the particles; following Heinz & Sunyaev 2003, we adopt $p = 2$. For an arbitrary X-ray emission process, we can assume $L_X \propto \dot{M}^q$, where q is a number that parameterizes the radiative efficiency of the X-ray process²³ (i.e., $q \neq 1$ indicates a nonthermal or inefficient mechanism). Thus, the measured slope of the L_R – L_X correlation can be written as

$$m = \frac{\frac{17}{12} - \frac{2}{3}\alpha}{q}. \quad (1)$$

For $m = 0.52 \pm 0.07$ and $\bar{\alpha} = 0.24 \pm 0.06$ (i.e., the weighted-average radio spectral index during our campaign), we find on average during the two decays that $q = 2.4 \pm 0.3$. Thus, we require a radiatively inefficient source of X-ray emission.

Given our empirical constraint on the radiative efficiency (through the q parameter), we can make some inferences on the most likely source of X-ray emission. Inverse Comptonization or SSC processes in an RIAF can readily produce the observed X-ray signatures. As the accretion rate drops, one expects the density of the inner region of the accretion flow to decrease. In turn, the optical depth to inverse-Compton scattering may then decrease and yield a gradual increase in Γ (e.g., Esin et al. 1997).

In terms of jet origins for X-ray emission, we describe below that most scenarios are unlikely, except perhaps in some instances of jet-related SSC emission, which is difficult to distinguish from SSC originating from an RIAF. As expanded upon below, different mechanisms for (jet) X-ray emission are expected to emit with different radiative efficiencies. Thus, in the following, we walk through different scenarios for jet emission, and in order for a scenario to be deemed viable, its predictions must be consistent with our observations on the average radio spectral index, with the observed evolution in Γ , and with the behavior in L_R – L_X .

²³ We make the assumption that the bolometric correction is constant with changing \dot{M} .

Since we have a precise measurement of the average radio spectral index, our combined constraints on the X-ray spectral softening and L_R – L_X allow us to exclude other scenarios for jet-dominated X-rays. However, the following discussion comes with the caveat that we assume that changes in radio/X-ray luminosities are driven primarily by changes in \dot{M} . If we assume that X-rays are always dominated by optically thin synchrotron radiation (again, emitted by a nonthermal electron population described by $dn/d\gamma \propto \gamma^{-p}$), then the X-ray spectral softening from $\Gamma = 1.5$ to 2 (as seen during the reflare) could be explained as optically thin synchrotron emission emanating from particles evolving to a steeper nonthermal distribution ($p = 2\Gamma - 1$ evolving from 2 to 3). Then, according to Equation 17(c) of Heinz & Sunyaev (2003), we would expect the slope of the L_R – L_X correlation to evolve from 0.7 to 0.6 in coordination with the X-ray spectrum softening from $\Gamma = 1.5$ to 2.0 (again, adopting a radio spectral index of $\bar{\alpha} = 0.24 \pm 0.06$). Therefore, if p were truly evolving to a steeper distribution, then we would expect to see the L_R – L_X slope become shallower as the source decays to quiescence, an effect that does not appear to be seen in Figure 4.

From L_R – L_X we can also exclude the possibility that the X-ray spectral softening is caused by a synchrotron-cooled jet dominating the X-rays. If this were the case, we would expect the transition to occur at $L_X \approx 10^{34} \text{ erg s}^{-1}$ (i.e., the luminosity at which Γ reaches 2), at which point the radiative efficiency would be $q_{\text{cool}} = p + 2 - \left(\frac{3}{2}\right)\Gamma$ (Heinz 2004; see also Section 4.2 of Plotkin et al. 2017b). For $p = 2$ as expected for a distribution of synchrotron-emitting particles for which we measure $\Gamma = 1.5$ at its hardest ($p = 2\Gamma - 1$; see also, e.g., Heinz & Sunyaev 2003), the radiative efficiency would be $q_{\text{cool}} = 1$. Adopting the weighted-average value of $\bar{\alpha} = 0.24 \pm 0.06$ and the weighted average of all measured values of Γ at luminosities $L_X \leq 10^{34} \text{ erg s}^{-1}$ ($\Gamma = 1.99 \pm 0.09$), we would therefore expect to see the slope of the L_R – L_X correlation increase to $m = 1.23 \pm 0.12$ at $L_X = 10^{34} \text{ erg s}^{-1}$ (Yuan & Cui 2005). In Figure 4 we show that all of the lowest radio luminosity data points lie above the expected synchrotron cooling decay, so we can likely rule it out.

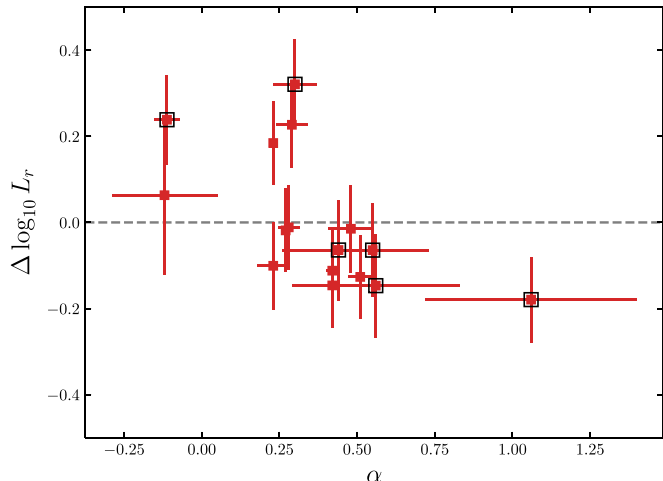


Figure 5. Logarithmic radio luminosity residuals vs. radio spectral index. We define the residuals as the difference between $\log_{10} L_R$ and its expected (logarithmic) value according to the best-fit L_R – L_X correlation. As in Figure 4, the black boxes highlight the observations taken during the decay of the first reflare.

Though we have ruled out the majority of pure jet models for the X-ray emission, we still identify a jet origin for SSC emission as a possibility. Jet SSC emission could plausibly come from either a thermal or a nonthermal particle distribution. A softening might then be expected if the Comptonized spectrum is produced by single scatterings of synchrotron-cooled seed photons (see, e.g., Corbel et al. 2008; Plotkin et al. 2017b, for discussions). However, confirming or refuting this scenario requires numerical modeling that is outside the scope of this paper. This would allow us to understand how the extra source of cooling would affect particle energies and therefore the power and spectrum of the seed synchrotron photons, as well as the average number of scatterings before inverse-Comptonized photons escape, and so on. In lieu of such modeling, for the time being we believe that an RIAF origin for the X-ray emission is the most reasonable.

4.3.1. Deviations from L_R – L_X

We stress that our best-fit slope only describes the *average* path taken through the L_R – L_X plane, since we observe temporary deviations about our best-fit line (which our regression technique models as intrinsic scatter). Similar deviations have also been seen for GX 339–4, and they illustrate the importance of measuring L_R – L_X slopes over a wide dynamic range in luminosity (see Section 4.2.3 of Corbel et al. 2013 for a detailed discussion). In Figure 5 we plot the (logarithmic) radio luminosity residuals against α and find a marginal possibility of an anticorrelation. We calculate a Spearman correlation coefficient $\rho = -0.5 \pm 0.2$, which we find has an $\sim 2\%$ probability of occurring by chance in randomly shuffled data (see Section 4.2 for our methodology).

Although we do not consider this to be a statistically significant anticorrelation, it is an intriguing result that warrants further observational scrutiny (on future outburst decays). Deviations from a simple Blandford & Königl (1979) compact jet can result in changes in α , which would then cause an anticorrelation between α and m (e.g., according to Equation (1), if α increases, then m decreases; also see Corbel et al. 2013 for a discussion on how α can influence a source’s position in the L_R – L_X plane). Thus, if the anticorrelation is indeed real, it may not be unexpected, and it could be manifesting itself as the

(observed) deviations from the global L_R – L_X correlation. Unfortunately, we cannot quantify if α really is the driver because we are not able to make precise-enough measurements of the slopes of individual deviations (since they cover too little dynamic range in luminosity) to directly compare changes in m to changes in α . Nevertheless, Figure 5 motivates the importance of obtaining meaningful constraints on α during high-cadence multiwavelength monitoring of future outburst decays.

5. Summary and Conclusions

We presented high-cadence, quasi-simultaneous X-ray and radio spectral monitoring of the BH-LMXB MAXI J1820+070 during the decline of its 2018 outburst and of a subsequent reflare. We find that, similar to previous observations of BH-LMXBs as they approach quiescence, the X-ray spectrum softened from $\Gamma \sim 1.7$ to $\Gamma \sim 2$ over the course of ~ 30 days, “saturating” at $\Gamma \sim 2$ even as the luminosity continued to decrease below $L_X \lesssim 10^{34}$ erg s $^{-1}$ ($10^{-5} L_{\text{Edd}}$). During this time, the radio spectrum generally remained slightly inverted, as the source luminosity decreased, with occasional deviations to a negative slope. However, the radio spectrum never reached values indicative of optically thin synchrotron emission.

We find that MAXI J1820+070 follows a correlation in the L_R – L_X plane of the form $L_R \propto L_X^{0.52 \pm 0.07}$, meaning that it is the fourth BH-LMXB, after GX 339–4, XTE J1118+480, and V404 Cygni, to follow the standard track over $\gtrsim 4$ decades in L_X . We use the slope of the L_R – L_X correlation, along with the average radio spectral index $\bar{\alpha} = 0.24 \pm 0.06$, to estimate the radiative efficiency parameter q . We find, on average, $q = 2.4 \pm 0.3$ over the two decays, suggesting that the X-ray emission is produced by a radiatively inefficient mechanism. The calculated value of q allows us to rule out particle acceleration along the jet becoming less efficient as the emission process responsible for the observed X-ray softening. The fact that the L_R – L_X slope remains steady and does not steepen at 10^{34} erg s $^{-1}$ also allows us to effectively exclude a synchrotron-cooled jet as the cause of the softening.

Excluding these jet origins for the X-ray emission implies that the dominant mechanism responsible for the observed softening is either Comptonization processes happening within an RIAF or possibly SSC processes from within the jet. MAXI J1820+070 is one of only two BH-LMXBs (the other being V404 Cygni) that have both good coverage in the L_R – L_X plane and a well-constrained distance (Atri et al. 2020), making this an important data set for studying BH-LMXBs during their decay to quiescence, as we have strong constraints on its luminosity. In the future, high-spectral-quality, strictly simultaneous radio and X-ray observations of other *nearby* transients (with low column density) are needed to eventually build population studies, in order to understand which details of the transition to quiescence are universal, and which details instead depend on system parameters (e.g., orbital period, donor mass) and disk/jet couplings (i.e., radio/X-ray luminosity correlation slope) that are specific to individual systems.

We thank the anonymous referee for useful comments that have helped improve the manuscript. A.W.S. would like to thank Bailey Tetarenko for useful discussions regarding the X-ray decay. A.W.S. would also like to thank Arash Bahramian for providing access to their exhaustive library of L_R – L_X data for BH-LMXBs. J.C.A.M.-J. was the recipient of an Australian Research Council Future Fellowship (FT140101082), funded by

the Australian government. P.K., E.G., and J.H. acknowledge financial support that was provided by the National Aeronautics and Space Administration through Chandra Award Nos. GO8-19033X, GO8-19027B, and GO9-20027B issued by the Chandra X-ray Center, which is operated by the Smithsonian Astrophysical Observatory for and on behalf of the National Aeronautics Space Administration under contract NAS8-03060. This work made use of data supplied by the UK Swift Science Data Centre at the University of Leicester. The scientific results reported in this article are based to a significant degree on observations made by the Chandra X-ray Observatory. This research has made use of data and software provided by the High Energy Astrophysics Science Archive Research Center (HEASARC), which is a service of the Astrophysics Science Division

at NASA/GSFC. The National Radio Astronomy Observatory is a facility of the National Science Foundation operated under cooperative agreement by Associated Universities, Inc.

Facilities: CXO, NICER, Swift, VLA.

Software: CASA (McMullin et al. 2007), CIAO (Fruscione et al. 2006), HEASoft (<https://heasarc.gsfc.nasa.gov/lheasoft/>), LinMix (Kelly 2007, <https://linmix.readthedocs.io/en/latest/>), UVMULTIFIT (Martí-Vidal et al. 2014), XSPEC (Arnaud 1996).

Appendix Observation Summary Tables

Tables A1 and A2 detail all X-ray and radio observations utilized in this work, including best-fit spectral measurements.

Table A1
Summary of X-Ray Observations and Best-fit Spectral Measurements

Instrument	ObsID	MJD ^a	t_{exp} (ks)	Net Count Rate ^b (count s ⁻¹)	Γ	$\log_{10} L_X(1-10 \text{ keV})$ (erg s ⁻¹)	W/dof ^c
(1)	(2)	(3)	(4)	(5)	(6)	(7)	(8)
Swift/XRT-WT	00010627109	58397.09	1.0	80.52	$1.66 \pm 0.02^{\text{d}}$	36.5 ± 0.1	654/640
Swift/XRT-WT	00010627110	58400.01	0.6	37.09	$1.63 \pm 0.03^{\text{e}}$	36.2 ± 0.1	470/461
Swift/XRT-WT	00010627111	58402.28	0.6	24.41	$1.59 \pm 0.04^{\text{f}}$	36.0 ± 0.1	401/383
Swift/XRT-WT	00010627112	58404.26	1.0	12.98	1.63 ± 0.02	35.9 ± 0.1	397/375
Swift/XRT-WT	00010627113	58406.73	0.9	13.85	1.60 ± 0.02	35.8 ± 0.1	433/375
Swift/XRT-WT	00010627114	58408.25	1.0	12.64	1.58 ± 0.02	35.8 ± 0.1	360/372
Swift/XRT-WT	00010627115	58410.30	1.3	10.21	1.65 ± 0.02	35.6 ± 0.1	426/381
Swift/XRT-WT	00010627116	58412.03	1.7	7.94	1.58 ± 0.02	35.6 ± 0.1	392/390
Swift/XRT-WT	00010627119	58417.48	6.9	4.03	1.64 ± 0.02	35.4 ± 0.1	470/503
Swift/XRT-WT	00010627120	58419.61	12.5	3.91	1.67 ± 0.01	35.3 ± 0.1	634/578
Swift/XRT-WT	00010627121	58422.27	2.0	3.41	1.70 ± 0.03	35.2 ± 0.1	296/271
Swift/XRT-WT	00010627122	58424.66	2.0	2.61	1.73 ± 0.04	35.1 ± 0.1	264/234
Swift/XRT-WT	00010627123	58425.46	1.4	2.58	1.74 ± 0.05	35.0 ± 0.1	163/183
Swift/XRT-WT	00010627124	58426.65	0.7	2.49	1.74 ± 0.07	35.0 ± 0.1	75/100
Swift/XRT-WT	00010627125	58428.17	2.2	2.12	1.77 ± 0.04	34.9 ± 0.1	202/222
Swift/XRT-WT	00010627126	58430.70	1.6	0.90	1.79 ± 0.08	34.8 ± 0.1	92/83
Swift/XRT-WT	00010627127	58432.55	0.4	1.27	1.74 ± 0.14	34.7 ± 0.1	29/31
Swift/XRT-WT	00010627128	58434.35	2.0	1.09	1.80 ± 0.06	34.6 ± 0.1	146/119
Chandra/ACIS-S	20207	58435.77	0.3 ^g	3.08	1.73 ± 0.10	34.6 ± 0.1	66/52
Swift/XRT-WT	00010627129	58436.53	1.9	0.74	1.75 ± 0.08	34.5 ± 0.1	95/82
Swift/XRT-WT	00010627130	58438.59	1.6	0.57	1.79 ± 0.10	34.4 ± 0.1	44/59
Swift/XRT-WT	00010627131	58440.19	1.7	0.53	$1.70^{+0.11}_{-0.10}$	34.3 ± 0.1	60/55
Chandra/ACIS-S	20186	58441.11	8.2	0.19	1.84 ± 0.07	34.2 ± 0.1	416/438
NICER/XTI	12001203010	58441.26	0.5	8.42	1.88 ± 0.04	34.3 ± 0.1	148/128
NICER/XTI	12001203012	58443.84	1.2	5.22	1.97 ± 0.04	34.0 ± 0.1	198/176
Chandra/ACIS-S	20208	58518.61	19.1	0.06	1.84 ± 0.10	32.9 ± 0.1	48/59
Chandra/ACIS-S	22080	58519.12	19.1	0.04	1.96 ± 0.11	32.7 ± 0.1	37/47
Swift/XRT-WT	00010627145	58563.12	1.1	19.46	1.54 ± 0.02	36.0 ± 0.1	523/472
Swift/XRT-WT	00010627146	58564.25	1.0	16.78	1.49 ± 0.02	35.9 ± 0.1	421/444
Swift/XRT-WT	00010627147	58565.18	1.0	14.13	1.53 ± 0.02	35.9 ± 0.1	422/408
Swift/XRT-WT	00010627148	58566.24	2.0	16.32	1.51 ± 0.01	35.9 ± 0.1	550/555
Swift/XRT-WT	00010627149	58567.17	2.1	14.51	1.55 ± 0.02	35.9 ± 0.1	525/531
Swift/XRT-WT	00010627150	58571.03	0.6	12.29	1.52 ± 0.03	35.8 ± 0.1	276/298
Swift/XRT-WT	00010627151	58572.15	1.0	11.83	1.58 ± 0.02	35.7 ± 0.1	398/365
Swift/XRT-WT	00010627152	58573.34	0.7	11.28	1.62 ± 0.03	35.7 ± 0.1	286/301
Swift/XRT-WT	00010627153	58574.33	1.0	11.09	1.62 ± 0.03	35.7 ± 0.1	402/357
Swift/XRT-WT	00010627154	58575.14	1.0	10.21	1.61 ± 0.03	35.7 ± 0.1	341/336
Swift/XRT-WT	00010627155	58576.06	0.1	8.67	1.64 ± 0.08	35.6 ± 0.1	73/73
Swift/XRT-WT	00010627156	58577.05	0.6	8.49	1.62 ± 0.04	35.6 ± 0.1	222/225
Swift/XRT-WT	00010627158	58583.17	0.7	3.00	1.61 ± 0.06	35.3 ± 0.1	140/118
Swift/XRT-WT	00010627159	58584.70	0.8	4.08	1.69 ± 0.05	35.2 ± 0.1	159/169
Swift/XRT-WT	00010627161	58586.68	0.9	1.07	1.66 ± 0.10	35.0 ± 0.1	45/58
Swift/XRT-WT	00010627162	58588.81	0.8	2.54	1.72 ± 0.06	35.0 ± 0.1	145/117

Table A1
(Continued)

Instrument	ObsID	MJD ^a	t_{exp} (ks)	Net Count Rate ^b (count s ⁻¹)	Γ	$\log_{10} L_X(1\text{-}10 \text{ keV})$ (erg s ⁻¹)	W/dof^c
(1)	(2)	(3)	(4)	(5)	(6)	(7)	(8)
Swift/XRT-WT	00010627163	58590.81	1.0	1.96	1.63 ± 0.06	34.9 ± 0.1	130/113
Chandra/ACIS-S	21200	58603.13	3.7	0.12	1.97 ± 0.14	34.0 ± 0.1	207/260
Chandra/ACIS-S	21201	58609.33	8.2	0.02	2.19 ± 0.23	33.2 ± 0.1	127/126
Chandra/ACIS-S	21202	58618.67	4.8	0.04	$1.99^{+0.24}_{-0.23}$	32.7 ± 0.1	103/122
Chandra/ACIS-S	21203	58627.42	11.4	0.05	1.95 ± 0.15	32.8 ± 0.1	25/31
Chandra/ACIS-S	21204	58636.67	28.2	0.03	2.11 ± 0.12	32.6 ± 0.1	44/50
Chandra/ACIS-S	21205	58645.08	65.6	0.03	2.04 ± 0.07	32.6 ± 0.1	121/103

Notes.^a MJD at the start of the observation.^b The typical uncertainty on net count rate is ~ 0.1 count s⁻¹.^c Cash (1979) statistic, modified for background-subtracted spectra.^d Best-fit spectrum included a diskbb component with $kT = 0.18$ keV.^e Best-fit spectrum included a diskbb component with $kT = 0.13$ keV.^f Best-fit spectrum included a diskbb component with $kT = 0.17$ keV.^g Effective exposure time for the readout streak.

Table A2
Summary of Radio Observations and Best-fit Spectral Measurements

Instrument/Configuration	Program ID	MJD ^a	t_{exp}^b (min)	α	$f_R(6 \text{ GHz})$ (mJy)	$\log_{10} L_R(5 \text{ GHz})$ (erg s ⁻¹)
(1)	(2)	(3)	(4)	(5)	(6)	(7)
VLA/D	18A-277	58398.04	11	0.230 ± 0.004	16.99 ± 0.03	30.0 ± 0.1
VLA/D	18A-277	58399.99	4	0.27 ± 0.01	7.46 ± 0.05	29.6 ± 0.1
VLA/D	18A-277	58402.85	4	0.42 ± 0.02	5.12 ± 0.03	29.5 ± 0.1
VLA/D	18A-277	58403.91	1	0.51 ± 0.04	4.20 ± 0.04	29.4 ± 0.1
VLA/D	18A-277	58405.90	1	0.42 ± 0.05	3.59 ± 0.05	29.3 ± 0.1
VLA/D	18A-277	58409.83	1	0.23 ± 0.05	3.19 ± 0.05	29.3 ± 0.1
VLA/D	18A-277	58418.85	3	0.28 ± 0.03	2.49 ± 0.03	29.2 ± 0.1
VLA/D	SK0335	58431.85	31	0.48 ± 0.07	1.38 ± 0.07	28.9 ± 0.1
VLA/C	SJ0238	58440.90	36	0.29 ± 0.05	1.16 ± 0.01	28.8 ± 0.1
VLA/C	18A-277	58473.68	19	0.50 ± 0.50	0.14 ± 0.01	27.9 ± 0.2
VLA/C	18A-277	58479.64	19	0.67 ± 0.50	0.15 ± 0.01	27.9 ± 0.1
VLA/C	18A-277	58484.75	19	-0.32 ± 0.32	0.15 ± 0.01	28.0 ± 0.2
VLA/C	SK0335	58516.70	38	-0.12 ± 0.17	0.156 ± 0.004	28.0 ± 0.2
VLA/B	SK0114	58603.32	36	-0.11 ± 0.04	0.88 ± 0.01	28.8 ± 0.1
VLA/B	SK0114	58608.35	36	0.30 ± 0.07	0.437 ± 0.004	28.4 ± 0.1
VLA/B	SK0114	58618.34	83	0.55 ± 0.18	0.108 ± 0.003	27.8 ± 0.1
VLA/B	SK0114	58627.34	83	0.44 ± 0.18	0.115 ± 0.003	27.8 ± 0.1
VLA/B	SK0114	58636.26	83	0.56 ± 0.27	0.076 ± 0.003	27.6 ± 0.1
VLA/B	SK0114	58645.24	83	1.06 ± 0.34	0.078 ± 0.004	27.6 ± 0.1

Notes.^a MJD at the start of the observation.^b On-source time, not removing time lost to flagging.**ORCID iDs**

- A. W. Shaw [ID](https://orcid.org/0000-0002-8808-520X) <https://orcid.org/0000-0002-8808-520X>
- R. M. Plotkin [ID](https://orcid.org/0000-0002-7092-0326) <https://orcid.org/0000-0002-7092-0326>
- J. C. A. Miller-Jones [ID](https://orcid.org/0000-0003-3124-2814) <https://orcid.org/0000-0003-3124-2814>
- J. Homan [ID](https://orcid.org/0000-0001-8371-2713) <https://orcid.org/0000-0001-8371-2713>
- E. Gallo [ID](https://orcid.org/0000-0001-5802-6041) <https://orcid.org/0000-0001-5802-6041>
- D. M. Russell [ID](https://orcid.org/0000-0002-3500-631X) <https://orcid.org/0000-0002-3500-631X>
- J. A. Tomsick [ID](https://orcid.org/0000-0001-5506-9855) <https://orcid.org/0000-0001-5506-9855>
- P. Kaaret [ID](https://orcid.org/0000-0002-3638-0637) <https://orcid.org/0000-0002-3638-0637>

S. Corbel [ID](https://orcid.org/0000-0001-5538-5831) <https://orcid.org/0000-0001-5538-5831>M. Espinasse [ID](https://orcid.org/0000-0001-9075-1489) <https://orcid.org/0000-0001-9075-1489>J. Bright [ID](https://orcid.org/0000-0002-7735-5796) <https://orcid.org/0000-0002-7735-5796>**References**

- Adachi, R., Murata, K. L., Oeda, M., et al. 2020, ATel, 13502, 1
- Armas Padilla, M., Degenaar, N., Russell, D. M., & Wijnands, R. 2013, MNRAS, 428, 3083

- Arnaud, K. A. 1996, in ASP Conf. Ser. 101, Astronomical Data Analysis Software and Systems V, ed. G. H. Jacoby & J. Barnes (San Francisco, CA: ASP), 17
- Atri, P., Miller-Jones, J. C. A., Bahramian, A., et al. 2020, *MNRAS*, 493, L81
- Baglio, M. C., Russell, D. M., & Lewis, F. 2018, ATel, 11418, 1
- Bahramian, A., Miller-Jones, J., Strader, J., et al. 2018, Radio/X-ray correlation database for X-ray binaries v0.1, Zenodo, doi:10.5281/zenodo.1252036
- Belloni, T. M. 2010, in States and Transitions in Black Hole Binaries, ed. T. Belloni, Vol. 794 (Berlin: Springer), 53
- Beri, A., Tetarenko, B. E., Bahramian, A., et al. 2019, *MNRAS*, 485, 3064
- Blandford, R. D., & Begelman, M. C. 1999, *MNRAS*, 303, L1
- Blandford, R. D., & Königl, A. 1979, *ApJ*, 232, 34
- Bright, J., Fender, R., & Motta, S. 2018, ATel, 11420, 1
- Bright, J. S., Fender, R. P., Motta, S. E., et al. 2020, *NatAs*, 4, 697
- Burrows, D. N., Hill, J. E., Nosek, J. A., et al. 2005, *SSRv*, 120, 165
- Canizares, C. R., Davis, J. E., Dewey, D., et al. 2005, *PASP*, 117, 1144
- Casares, J., Charles, P. A., & Naylor, T. 1992, *Natur*, 355, 614
- Cash, W. 1979, *ApJ*, 228, 939
- Connors, R. M. T., Markoff, S., Nowak, M. A., et al. 2017, *MNRAS*, 466, 4121
- Corbel, S., Coriat, M., Brocksopp, C., et al. 2013, *MNRAS*, 428, 2500
- Corbel, S., & Fender, R. P. 2002, *ApJL*, 573, L35
- Corbel, S., Fender, R. P., Tomsick, J. A., Tzioumis, A. K., & Tingay, S. 2004, *ApJ*, 617, 1272
- Corbel, S., Koerding, E., & Kaaret, P. 2008, *MNRAS*, 389, 1697
- Corbel, S., Tomsick, J. A., & Kaaret, P. 2006, *ApJ*, 636, 971
- Coriat, M., Corbel, S., Prat, L., et al. 2011, *MNRAS*, 414, 677
- Corral-Santana, J. M., Casares, J., Muñoz-Darias, T., et al. 2013, *Sci*, 339, 1048
- Denisenko, D. 2018, ATel, 11400, 1
- Done, C., Gierliński, M., & Kubota, A. 2007, *A&ARv*, 15, 1
- Dzib, S. A., Massi, M., & Jaron, F. 2015, *A&A*, 580, L6
- Esin, A. A., McClintock, J. E., & Narayan, R. 1997, *ApJ*, 489, 865
- Espinasse, M., Corbel, S., Kaaret, P., et al. 2020, *ApJL*, 895, L31
- Espinasse, M., & Fender, R. 2018, *MNRAS*, 473, 4122
- Fabian, A. C., Buisson, D. J., Kosec, P., et al. 2020, *MNRAS*, 493, 5389
- Fender, R. P. 2001, *MNRAS*, 322, 31
- Fender, R. P., Gallo, E., & Jonker, P. G. 2003, *MNRAS*, 343, L99
- Fender, R. P., Hjellming, R. M., Tilanus, R. P. J., et al. 2001, *MNRAS*, 322, L23
- Fruscione, A., McDowell, J. C., Allen, G. E., et al. 2006, *Proc. SPIE*, 6270, 62701V
- Gallo, E., Degenaar, N., & van den Eijnden, J. 2018, *MNRAS*, 478, L132
- Gallo, E., Fender, R. P., Miller-Jones, J. C. A., et al. 2006, *MNRAS*, 370, 1351
- Gallo, E., Miller, B. P., & Fender, R. 2012, *MNRAS*, 423, 590
- Gallo, E., Miller-Jones, J. C. A., Russell, D. M., et al. 2014, *MNRAS*, 445, 290
- Garmire, G. P., Bautz, M. W., Ford, P. G., Nosek, J. A., & Ricker, G. R. J. 2003, *Proc. SPIE*, 4851, 28
- Gendreau, K. C., Arzoumanian, Z., Adkins, P. W., et al. 2016, *Proc. SPIE*, 9905, 99051H
- Hambach, J., Ulowetz, J., Vanmunster, T., Cejudo, D., & Patterson, J. 2019, ATel, 13014, 1
- Heinz, S. 2004, *MNRAS*, 355, 835
- Heinz, S., & Sunyaev, R. A. 2003, *MNRAS*, 343, L59
- HI4PI Collaboration, Ben Bekhti, N., Flöer, L., et al. 2016, *A&A*, 594, A116
- Homan, J., Bright, J., Motta, S. E., et al. 2020, *ApJL*, 891, L29
- Jones, F. C., & Ellison, D. C. 1991, *SSRv*, 58, 259
- Kajava, J. J. E., Motta, S. E., Sanna, A., et al. 2019, *MNRAS*, 488, L18
- Kajava, J. J. E., Veledina, A., Tsygankov, S., & Neustroev, V. 2016, *A&A*, 591, A66
- Kalemci, E., Tomsick, J. A., Buxton, M. M., et al. 2005, *ApJ*, 622, 508
- Kara, E., Steiner, J. F., Fabian, A. C., et al. 2019, *Natur*, 565, 198
- Kawamuro, T., Negoro, H., Yoneyama, T., et al. 2018, ATel, 11399, 1
- Kelly, B. C. 2007, *ApJ*, 665, 1489
- Kochanek, C. S., Shappee, B. J., Stanek, K. Z., et al. 2017, *PASP*, 129, 104502
- Kong, A. K. H., McClintock, J. E., Garcia, M. R., Murray, S. S., & Barret, D. 2002, *ApJ*, 570, 277
- Maccarone, T. J. 2005, *MNRAS*, 360, L68
- Malzac, J., Belmont, R., & Fabian, A. C. 2009, *MNRAS*, 400, 1512
- Markoff, S., Falcke, H., & Fender, R. 2001, *A&A*, 372, L25
- Markoff, S., Nowak, M., Corbel, S., Fender, R., & Falcke, H. 2003, *A&A*, 397, 645
- Markoff, S., Nowak, M. A., & Wilms, J. 2005, *ApJ*, 635, 120
- Marti-Vidal, I., Vlemmings, W. H. T., Muller, S., & Casey, S. 2014, *A&A*, 563, A136
- Matsuoka, M., Kawasaki, K., Ueno, S., et al. 2009, *PASJ*, 61, 999
- McMullin, J. P., Waters, B., Schiebel, D., Young, W., & Golap, K. 2007, in ASP Conf. Ser. 376, Astronomical Data Analysis Software and Systems XVI, ed. R. A. Shaw, F. Hill, & D. J. Bell (San Francisco, CA: ASP), 127
- Miller, J. M., Homan, J., Steeghs, D., et al. 2006, *ApJ*, 653, 525
- Narayan, R., & McClintock, J. E. 2008, *NewAR*, 51, 733
- Orosz, J. A., Jain, R. K., Bailyn, C. D., McClintock, J. E., & Remillard, R. A. 1998, *ApJ*, 499, 375
- Perley, R. A., & Butler, B. J. 2017, *ApJS*, 230, 7
- Plotkin, R. M., Bright, J., Miller-Jones, J. C. A., et al. 2017a, *ApJ*, 848, 92
- Plotkin, R. M., Gallo, E., & Jonker, P. G. 2013, *ApJ*, 773, 59
- Plotkin, R. M., Gallo, E., Markoff, S., et al. 2015, *MNRAS*, 446, 4098
- Plotkin, R. M., Markoff, S., Kelly, B. C., Körding, E., & Anderson, S. F. 2012, *MNRAS*, 419, 267
- Plotkin, R. M., Miller-Jones, J. C. A., Chomiuk, L., et al. 2019, *ApJ*, 874, 13
- Plotkin, R. M., Miller-Jones, J. C. A., Gallo, E., et al. 2017b, *ApJ*, 834, 104
- Rana, V., Loh, A., Corbel, S., et al. 2016, *ApJ*, 821, 103
- Reis, R. C., Fabian, A. C., & Miller, J. M. 2010, *MNRAS*, 402, 836
- Remillard, R. A., & McClintock, J. E. 2006, *ARA&A*, 44, 49
- Reynolds, M. T., & Miller, J. M. 2011, *ApJL*, 734, L17
- Reynolds, M. T., & Miller, J. M. 2013, *ApJ*, 769, 16
- Reynolds, M. T., Reis, R. C., Miller, J. M., Cackett, E. M., & Degenaar, N. 2014, *MNRAS*, 441, 3656
- Ribó, M., Munar-Adrover, P., Paredes, J. M., et al. 2017, *ApJL*, 835, L33
- Russell, D. M., Baglio, M. C., & Lewis, F. 2019, ATel, 12534, 1
- Russell, D. M., Markoff, S., Casella, P., et al. 2013, *MNRAS*, 429, 815
- Shappee, B. J., Prieto, J. L., Grupe, D., et al. 2014, *ApJ*, 788, 48
- Shidatsu, M., Nakahira, S., Yamada, S., et al. 2018, *ApJ*, 868, 54
- Sobolewska, M. A., Papadakis, I. E., Done, C., & Malzac, J. 2011, *MNRAS*, 417, 280
- Stiele, H., & Kong, A. K. H. 2020, *ApJ*, 889, 142
- Tetarenko, B. E., Sivakoff, G. R., Heinke, C. O., & Gladstone, J. C. 2016, *ApJS*, 222, 15
- Tomsick, J. A., Corbel, S., & Kaaret, P. 2001, *ApJ*, 563, 229
- Tomsick, J. A., Kalemci, E., & Kaaret, P. 2004, *ApJ*, 601, 439
- Torres, M. A. P., Casares, J., Jiménez-Ibarra, F., et al. 2019, *ApJL*, 882, L21
- Torres, M. A. P., Casares, J., Jiménez-Ibarra, F., et al. 2020, *ApJL*, 893, L37
- Tremou, E., Corbel, S., Fender, R. P., et al. 2020, *MNRAS*, 493, L132
- Tucker, M. A., Shappee, B. J., Hololen, T. W. S., et al. 2018, *ApJL*, 867, L9
- Ulowetz, J., Myers, G., & Patterson, J. 2019, ATel, 12567, 1
- Uttley, P., Gendreau, K., Markwardt, C., et al. 2018, ATel, 11423, 1
- Veledina, A., Poutanen, J., & Vurm, I. 2011, *ApJL*, 737, L17
- Wilms, J., Allen, A., & McCray, R. 2000, *ApJ*, 542, 914
- Xu, Y., Harrison, F. A., Tomsick, J. A., et al. 2020, *ApJ*, 893, 42
- Xue, Y. Q., & Cui, W. 2007, *A&A*, 466, 1053
- Yuan, F., & Cui, W. 2005, *ApJ*, 629, 408
- Yuan, F., & Narayan, R. 2014, *ARA&A*, 52, 529
- Zdziarski, A. A., Lubinski, P., Gilfanov, M., & Revnivtsev, M. 2003, *MNRAS*, 342, 355
- Zhang, G. B., Bernardini, F., Russell, D. M., et al. 2019, *ApJ*, 876, 5